AIAA JOURNAL
Vol. 44, No. 1, January 2006

e^N Transition Prediction in Three-Dimensional Boundary Layers on Inclined Prolate Spheroids

Hans W. Stock*
DLR, German Aerospace Center, 38108 Braunschweig, Germany

The capability of the e^N method to predict transition in complex three-dimensional, laminar boundary layers is demonstrated. Flows around inclined prolate spheroids are ideally suited for investigation because they exhibit highly divergent and convergent three-dimensional viscous flows on curved surfaces. The inviscid flowfield is described by the potential theory and the viscous layer by a three-dimensional laminar boundary-layer method. This approach is applied in weak viscous/inviscid interaction regions only, that is, in attached laminar flow regions, and validated by comparison with measured wall pressure and skin friction in magnitude and direction. For the determination of the transition location, the laminar boundary layer is analyzed by the two N factor e^N method. Excited Tollmien–Schlichting waves of constant frequencies and stationary crossflow waves of constant wavelength are computed by the local, linear stability theory. Both N factor integrations are executed along 21 streamlines, which regularly cover the surface of the prolate spheroid. First, the values of both N factors at the measured transition locations are calculated, which deliver the stability limit of the prolate spheroid in the considered wind tunnel. Second, based on the knowledge of the stability limit, the transition locations are evaluated. The prolate spheroid with an aspect ratio of 6:1 was tested in two wind tunnels at angles of attack from 0 to 30 deg and Reynolds numbers from 1.5×10^6 to 43×10^6. The measured transition locations compare remarkably well with computations for all investigated flow cases.

Nomenclature

a = major axis of the prolate spheroid
b = minor axis of the prolate spheroid
C_{ft} = resultant skin-friction coefficient
C_p = pressure coefficient
L = reference length, $2a$
N_{CF} = value of N^*_{CF} at measured transition
N_{TS} = value of N^*_{TS} at measured transition
N^*_{CF} = envelope N factors of unstable crossflow waves
N^*_{TS} = envelope N factors of unstable Tollmien–Schlichting waves
Re = Reynolds number based on freestream conditions and reference length, $U_\infty \varrho_\infty L/\mu_\infty$
$Re\delta^*_c$ = Reynolds number based on the displacement thickness of the crossflow velocity profile, $U_e \rho_e \delta^*_c/\mu_e$
$Re\delta^*_s$ = Reynolds number based on the displacement thickness of the streamwise velocity profile, $U_e \rho_e \delta^*_s/\mu_e$
U = velocity component in streamwise direction
u = velocity component in ξ' direction
V = velocity component in crossflow direction
v = velocity component in ϕ' direction
X, Y, Z = Cartesian coordinates, where X is in direction of the major axis of the prolate spheroid
X_0 = absolute value of X coordinate of the stagnation point
α = angle of attack
α' = angle between the velocity components u_e and v_e
γ = local wall shear stress direction relative to a line $\phi = \mathrm{const}$
δ^*_c = displacement thickness of the crossflow velocity profile, $-\int_0^\infty \frac{V}{U_e}\,\mathrm{d}\zeta$
δ^*_s = displacement thickness of the streamwise velocity profile, $\int_0^\infty \left(1 - \frac{U}{U_e}\right)\mathrm{d}\zeta$
λ = angle between the coordinates ξ' and ϕ'
μ = dynamic viscosity
ξ, ϕ, ζ = orthogonal, surface-oriented coordinates; ξ in azimuthal direction, ϕ in circumferential direction, ζ in wall normal direction
ξ', ϕ', ζ = transformed nonorthogonal, surface-oriented coordinates
ρ = density

Subscripts

e = at the outer edge of the boundary layer
∞ = upstream infinity

I. Introduction

LAMINAR flow technology is one of the major technologies in aeronautics and offers great potential for improvements for future commercial transport aircraft concerning the reduction of fuel consumption, environmental pollution, takeoff weight, and significant amelioration of cruise lift-to-drag ratio. To evaluate potential savings, one must be able to predict accurately the location of boundary-layer transition on wings, tails, nacelles, and possibly fuselages.

Transition is the result of complex phenomena, which depend on many parameters, such as Reynolds number, pressure gradient, wall temperature, wall mass transfer, disturbance environment, etc. The first stage of the transition process is characterized by the boundary-layer receptivity. This process describes the means by which the environmental disturbances (freestream turbulence, noise, vibration, surface roughness, waviness, etc.) trigger the laminar boundary layer to develop mechanisms that lead to transition. The way in which the

---

Received 9 February 2005; revision received 14 July 2005; accepted for publication 17 July 2005.

*Senior Research Scientist, Institute of Aerodynamics and Flow Technology, Lilienthalplatz 7; hans.w.stock@web.de.

initialized disturbances grow can be described by two different processes. First, if the amplitudes of the initialized disturbances are small, they are amplified linearly and close to the transition point their growth rate starts to be nonlinear (natural transition); second, if the initialized disturbances are not weak, nonlinear phenomena are immediately observed, transition occurs rapidly, and the linear growth rate of the disturbances is bypassed (bypass transition). In aerodynamic flows, that is, flows over wings, tails, and nacelles, transition is typically the result of natural transition. To the contrary, in turbomachinery applications, the main transition mechanism is bypass transition imposed on the boundary layer by high levels of turbulence in the freestream, coming from the upstream blade rows.[1,2]

Today the spectrum of available transition prediction methods extends from stability theories (e^N method) and transition prediction incorporated in turbulence models to direct numerical simulations (DNS) and large eddy simulations (LES). DNS and LES play an increasingly important role in the research of transition due to the development of new, extremly powerful computers and numerical algorithms.[3,4] Nevertheless, today the proper specification of the external disturbance level and structure poses substantial challenges.[5] In addition, DNS and LES are far too costly for engineering applications and are currently mainly used as research tools and substitutes for controlled experiments.

Attempts to incorporate transition prediction features in turbulence models were started almost 10 years ago.[5–10] The advantage of this approach, especially in modern general purpose computational fluid dynamics (CFD) codes, is that Reynolds-averaged Navier–Stokes (RANS) methods for complex geometries can be executed on unstructered grids using local operations only. Nonlocal operations, such as the evaluation of integral boundary-layer parameters or integration of quantities along the direction of external streamlines, are not requested. In addition, correlations can be developed for the different transition mechanisms, ranging from natural to bypass transition. The disadvantage of this approach is that up to now it has suffered from the lack of the evaluation of crossflow instabilities; only Tollmien–Schlichting perturbations are considered in three-dimensional flows. In addition, the computed transition locations depend on the settings of the turbulence quantities at the boundaries of the computational domain and the grid density near the wall.

The e^N method[11,12] is based on the linear stability theory of parallel flows. Here, the value of e^N stands for the ratio of the disturbance amplitude at transition related to the disturbance amplitude at the neutral point. The quantity N, representing the limiting N factor, is a priori not known and has to determined by analyzing wind-tunnel or free-flight tests; hence, in this aspect the e^N method is semi-empirical. Nevertheless, it represents the most frequently used transition prediction method for wings, tails, and nacelles in the aircraft industry.[13,14] For these aerodynamic components, only natural transition is of interest for both wind-tunnel experiment interpretation and free-flight simulations. The application of the e^N method to complex geometries, other than the already mentioned aircraft components, is extremely difficult. The wall layers, that is, the velocity profiles in the streamwise and crossflow directions have to be evaluated accurately either on viscous-adapted RANS grids or by boundary-layer solutions, using the pressure distribution from RANS solutions as boundary condition. On complex geometries, the computation of the laminar boundary-layer flow often poses problems and the approach relies solely on RANS solutions. The careful mesh-adaption procedure, on the other hand, represents an untolerable costly situation for both computational and engineering efforts.

The discussed approaches represent the essential parts of the transition modeling spectrum for the different applications areas and accuracy requirements. In conclusion, a rigorous modeling of the transition process up to now has not been available, but the e^N method still represents a practical approach and is an important design tool in aircraft industry, when coupled to RANS methods.

The e^N method was successfully applied in European programs for the analysis of free-flight test at subsonic and transonic speeds on laminar wing gloves using as a test bed the LFU-205,[15] the Dornier Do228,[16–18] VFW-614[19–21] [Advanced Technology Testing Aircraft System (ATTAS) program], the Fokker-100[22–24] [European Laminar Flow Technology (ELFIN) program], the Falcon,[25] and on a nacelle.[26,27] The important outcome of that activity was the existence of free-flight limiting N factors, which were introduced as stability limits in computational methods for the design of laminar gloves for the ATTAS wing,[28] the ELFIN wing,[29] the fin on the Airbus A320,[30] and the nacelle.[31,32] Contrary to the free-flight situation, the limiting N factors for wind tunnels are specific quantities depending on the flow quality of the considered facility. Examples for the evaluation of the limiting N factors in wind tunnels are the Soufflerie 1 Modane (S1MA) transonic facility[20] (ONERA, Modane, France), the DNW[15] (German Dutch Low Speed Tunnel, The Netherlands), the TWB[33] (Transonic Wind Tunnel at the DLR, German Aerospace Center, Braunschweig, Germany), the Royal Aircraft Establishment Bedford tunnel[34] (Great Britain), and the Arizona State University Unsteady Wind Tunnel (United States).[35]

Only recently, it has been shown that RANS methods coupled to the e^N transition prediction produce excellent results for laminar airfoils when compared to wind-tunnel measurements.[36–39] Subsequently, the coupling was extended to simple three-dimensional flows on infinite swept wing configurations, where the two N factor e^N method[40–42] was applied. Comparisons with measurements showed a remarkable agreement for situations where transition is provoked by both Tollmien–Schlichting and crossflow waves[43] and for pure crossflow-induced transition.[44] The common, primary goal in the preceeding publications was the validation of the coupling strategy of Navier–Stokes methods to the e^N method. Presently, the main emphasis is not the coupling strategy; to the contrary, the applicability of the e^N method to complex, three-dimensional, boundary-layer flows is of primary interest. To the author's knowledge this topic has not yet been presented in the open literature.

Flows around inclined prolate spheroids will be investigated, which represent a simple geometry but exhibit highly divergent and convergent three-dimensional viscous flows on curved surfaces. Here, the pressure distribution will be evaluated by the potential theory,[45] which is applied as boundary condition in a finite difference boundary-layer method for three-dimensional, laminar flows.[46]

II. Computational Procedure

A. Potential Flow and Coordinate System

The potential Φ for flows around prolate spheroids is described in orthogonal, surface oriented coordinates ξ and ϕ by[45] (Fig. 1a)

$$\Phi = -U_\infty(aK_1\cos\xi + bK_2\sin\xi\cos\phi) \tag{1}$$

where

$$K_1 = E_1\cos\alpha, \qquad K_2 = E_2\sin\alpha \tag{2}$$

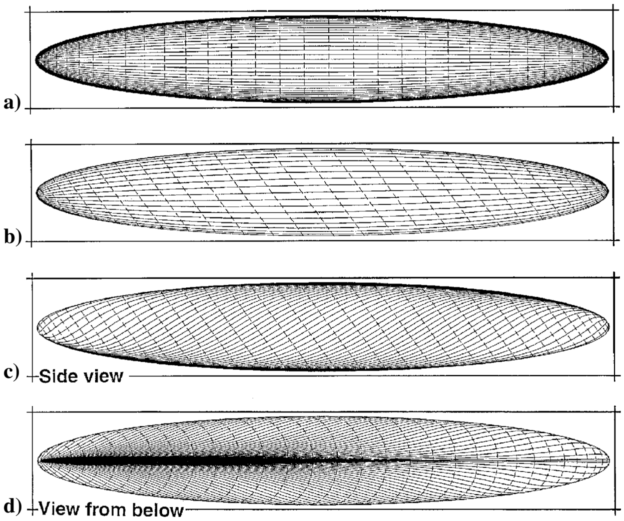

Fig. 1 Different coordinate systems for prolate spheroid at angle of attack $\alpha = 30$ deg: a) ——, $\phi = \text{const}$ and - - - -, $\xi = \text{const}$; b) ——, $\phi' = \text{const}$ and - - - -, $\xi' = \text{const}$; c) ——, streamlines and - - - -, $\xi' = \text{const}$; and d) ——, streamlines and - - - -, $\xi' = \text{const}$.

with

$$E_1 = 1 + \frac{(1/2e)\,\ln[(1+e)/(1-e)] - 1}{1/(1-e^2) - (1/2e)\,\ln[(1+e)/(1-e)]} \tag{3}$$

$$E_2 = \frac{2}{2 - 1/E_1} \tag{4}$$

$$e = \left[1 - \left(\frac{b}{a}\right)^2\right]^{\frac{1}{2}} \tag{5}$$

The relation between Cartesian coordinates and the orthogonal, surface-oriented coordinates is given by

$$X = -a\cos\xi, \qquad Y = -b\sin\xi\sin\phi, \qquad Z = -b\sin\xi\cos\phi \tag{6}$$

The ξ and ϕ orthogonal, surface-oriented coordinate system produces a geometric singularity in the poles of the prolate spheroid and an aerodynamic singularity in the stagnation point. To circumvent the computational difficulties, a transformed nonorthogonal, surface-oriented coordinate system, ξ' and ϕ', is proposed, which delivers the geometric and aerodynamic singularities concentrated in the stagnation point (Fig. 1). The lines $\xi' = \text{const}$ lie in planes that are parallel to the tangential plane in the stagnation point. The relation between the Cartesian coordinates and the transformed nonorthogonal, surface-oriented coordinates is given by

$$X = -B\cos\xi' + A\sin\xi'\cos\phi', \qquad Y = -b\sin\xi'\sin\phi'$$

$$Z = -D\cos\xi' - C\sin\xi'\sin\phi' \tag{7}$$

where

$$A = (b/a)(K_2/K_1)X_0, \qquad B = X_0$$

$$C = (b/a)X_0, \qquad D = (b^2/a)(K_2/K_1)X_0 \tag{8}$$

X_0 is the absolute value of the Cartesian coordinate X in the stagnation point and is given by

$$X_0 = \frac{a^2K_1}{\left(a^2K_1^2 + b^2K_2^2\right)^{\frac{1}{2}}} \tag{9}$$

The potential in the transformed, nonorthogonal, surface-oriented coordinate system simplifies to

$$\Phi = -U_\infty\left(a^2K_1\big/X_0\right)\cos\xi' \tag{10}$$

Hence, the lines $\xi' = \text{const}$ are equipotential lines. The velocity components in ξ' and ϕ' direction, u_e and v_e, respectively, and the angle α' can be evaluated by

$$u_e = \frac{h_2^2h_1}{q^2}\frac{\partial\Phi}{\partial\xi'}, \qquad v_e = -\frac{gh_2}{q^2}\frac{\partial\Phi}{\partial\xi'}, \qquad \alpha' = \sin^{-1}\left(\frac{v_e}{U_e}\sin\lambda\right) \tag{11}$$

with

$$q^2 = h_1^2h_2^2 - g^2$$

The angle λ can be calculated from

$$\cos\lambda = g/h_1h_2 \tag{12}$$

The metric coefficients h_1, h_2, and g are given by

$$h_1^2 = \left(\frac{\partial X}{\partial\xi'}\right)^2 + \left(\frac{\partial Y}{\partial\xi'}\right)^2 + \left(\frac{\partial Z}{\partial\xi'}\right)^2$$

$$h_2^2 = \left(\frac{\partial X}{\partial\phi'}\right)^2 + \left(\frac{\partial Y}{\partial\phi'}\right)^2 + \left(\frac{\partial Z}{\partial\phi'}\right)^2$$

$$g = \frac{\partial X}{\partial\xi'}\frac{\partial X}{\partial\phi'} + \frac{\partial Y}{\partial\xi'}\frac{\partial Y}{\partial\phi'} + \frac{\partial Z}{\partial\xi'}\frac{\partial Z}{\partial\phi'} \tag{13}$$

The resultant velocity U_e can be expressed by

$$U_e^2 = u_e^2 + v_e^2 + 2\cos\lambda u_e v_e \tag{14}$$

from which the pressure coefficient C_p is deduced:

$$C_p = 1 - (U_e/U_\infty)^2 \tag{15}$$

In addition, streamlines of the inviscid flow have to be calculated, along which the N factor integration is actually executed. Conventionally, the N factor integration is performed in the group velocity direction.[47] Because the group velocity direction is almost identical to the resultant velocity direction at the outer edge of the boundary layer, the difference in the computed N factors is correspondingly almost negligible.[48] Equation (11) is applied for the streamline computation using a simple finite difference scheme. The calculation is started in a plane that contains the center of the prolate spheroid, that is, at $\xi' = 90$ deg. There are 21 streamlines evaluated, including the windward streamline, $\phi' = 0$ deg, and leeward streamlines, $\phi' = 180$ deg. The values of the starting positions in ϕ' are chosen such that the body surface is regularly covered, that is,

$$\phi'_j = (j-1)\Delta\phi', \qquad j = 1, 21 \tag{16}$$

with $\Delta\phi' = 9$ deg. The streamline computation is executed from $\xi' = 90$ to $\xi' = 179$ deg, that is, close to the rearward stagnation point. Because of the symmetry of the flow, the streamlines from $\xi' = 1$ to $\xi' = 89$ deg are deduced by mirroring. The curvilinear coordinate S, which describes the position of the streamlines, is finally provided by discrete points in the Cartesian coordinate system:

$$S_{i,j} = f(X_{i,j}, Y_{i,j}, Z_{i,j}), \qquad i = 1, 179,\ j = 1, 21 \tag{17}$$

with $i = 1, \ldots, 179$, $j = 1, \ldots, 21$, where i is in the azimuthal and j in the circumferential direction. The integration step for the N factor integration, ΔS, is provided by

$$\Delta S_{i,j} = \left[(X_{i+1,j} - X_{i,j})^2 + (Y_{i+1,j} - Y_{i,j})^2 + (Z_{i+1,j} - Z_{i,j})^2\right]^{\frac{1}{2}} \tag{18}$$

To include curvature effects in the stability computation, the curvature of the streamlines (CS) has to be calculated and is given by

$$\mathrm{CS}_{i,j} = \left[\left(\frac{\partial^2 X_{i,j}}{\partial S_{i,j}^2}\right)^2 + \left(\frac{\partial^2 Y_{i,j}}{\partial S_{i,j}^2}\right)^2 + \left(\frac{\partial^2 Z_{i,j}}{\partial S_{i,j}^2}\right)^2\right]^{\frac{1}{2}} \tag{19}$$

Finally, the streamlines are shown in Fig. 1 in a side view and in a view from below for an angle of attack $\alpha = 30$ deg.

B. Boundary-Layer Computation

Basically, it is possible to execute the finite difference computation of the boundary layer[46] in streamline coordinates. Because of the high convergence and divergence of the flow, however, the computational mesh has to be rearranged continuously (Fig. 1). Hence, it is much easier to calculate the boundary-layer development in the ξ', ϕ' coordinate system and to interpolate the viscous-layer results for the stability analysis, that is, velocity profiles in streamwise- and crossflow directions, etc., onto the equivalent 21 streamline positions.

A rather fine surface mesh is applied with $\Delta\xi' = \Delta\phi' = 1$ deg, and in surface normal direction 121 mesh points are used. For the complete prolate spheroid, a total number of nearly 4 million mesh points is provided. The integration is started close to the foreward stagnation point, that is, $\xi' = 1$ deg, and continued to the location where the laminar boundary layer separates. For the actual prolate spheroid with an aspect ratio of 6:1 and small angles of attack $\alpha < 7$ deg, a closed separation line develops in the adverse pressure gradient region. For larger angles of attack, an open laminar free vortex-layer separation line develops on the sides of the body. The vortex-layer separation is provoked by the circumferential pressure distribution, which shifts the near-wall boundary-layer material upward from the windward symmetry plane and downward from the leeward symmetry plane. As a result, boundary-layer material is accumulated on the sides of the prolate spheroid. When the locally thickened laminar boundary layer is exposed to adverse, streamwise pressure gradients, the open free vortex-layer separation develops. The boundary-layer code[46] is capable to compute the complete region of attached laminar flow with the closed or open separation lines included.

C. Stability Analysis and Limiting *N* Factors

The boundary layers along the different streamlines are analyzed with the local, linear stability theory[47] using for the interpretation the two N factor e^N approach.[40–42] The excitation of Tollmien–Schlichting (TS) waves of constant frequency and stationary crossflow (CF) waves of constant, total wavelength is computed. In Refs. 43 and 44, stationary CF waves of constant spanwise wave numbers are used for infinite swept wing configurations. To the contrary, in fully three-dimensional situations, the application of constant total wavelengths appears physically more relevant. Nevertheless, note that the stability results for both constant spanwise wave number and constant total wavelength computations are almost identical.[48]

To begin, the measured transition locations, which are available in the X, ϕ coordinate system,[49,50] are interpolated onto the corresponding streamlines. The development of the envelope N factors of both TS and CF waves is evaluated along the discrete streamlines. Subsequently, the N^*_{TS} and N^*_{CF} factors at the measured transition locations, N_{TS} and N_{CF}, respectively, are determined. The mean values of the latter N factors represent the limiting N factors, from which the stability limit of the prolate spheroid in the considered wind tunnel is deduced. Finally, the knowledge of the stability limit allows the prediction of the transition locations.

In situations where the boundary layer is predicted to remain laminar up to separation, transition is assumed to occur at separation. The prediction of transition in laminar separation bubbles is beyond the scope of the present paper.

III. Results

A. Comparison with Measured Pressure and Wall Friction

The prolate spheroid of 2.4-m total length was tested in the DFVLR 3 × 3 Meter Low Speed Wind Tunnel Göttingen[49] at angles

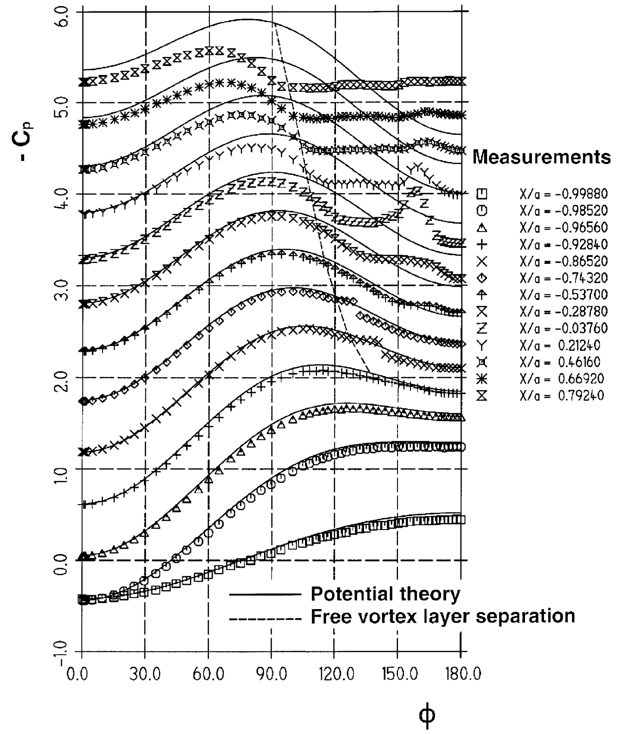

Fig. 3 Measured and computed pressure coefficient C_p on prolate spheroid for Reynolds number $Re = 1.53 \times 10^6$ and angle of attack $\alpha = 29.7$ deg.

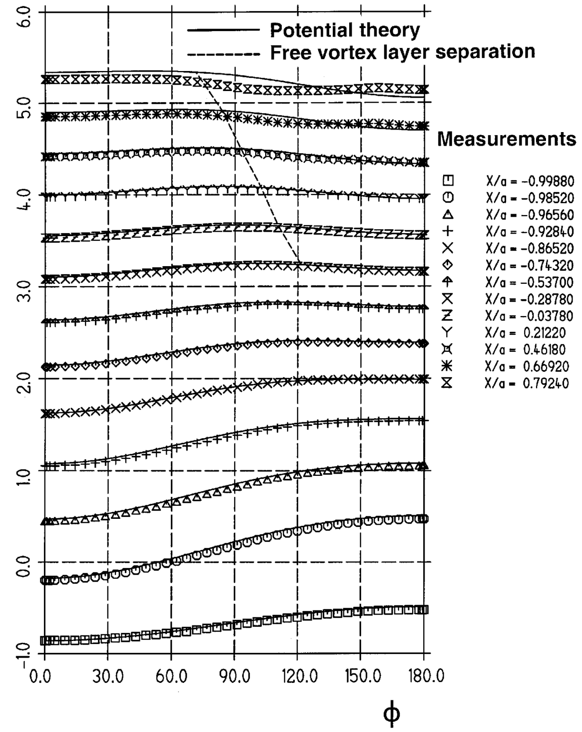

Fig. 2 Measured and computed pressure coefficient C_p on prolate spheroid for Reynolds number $Re = 1.52 \times 10^6$ and an angle of attack $\alpha = 10$ deg.

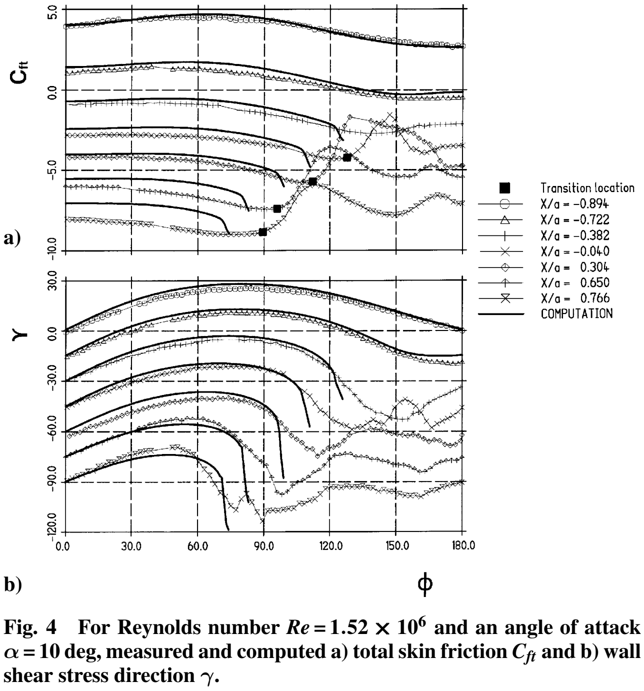

Fig. 4 For Reynolds number $Re = 1.52 \times 10^6$ and an angle of attack $\alpha = 10$ deg, measured and computed a) total skin friction C_{ft} and b) wall shear stress direction γ.

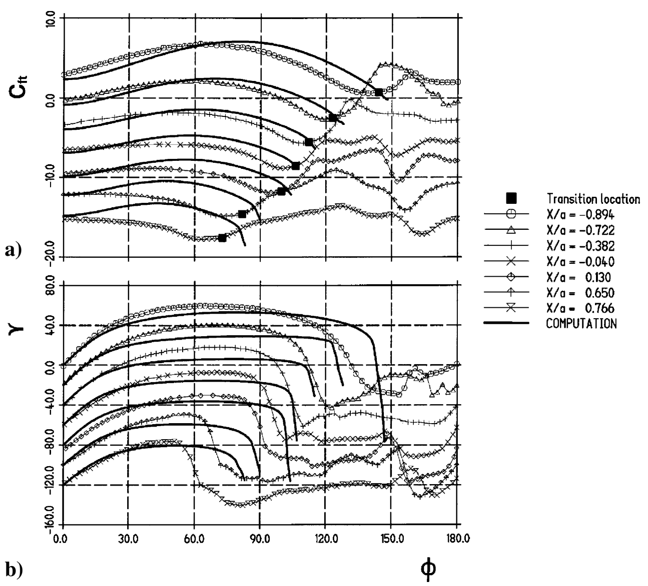

Fig. 5 For Reynolds number $Re = 1.53 \times 10^6$ and angle of attack $\alpha = 29.7$ deg, measured and computed a) total skin friction C_{ft} and b) wall shear stress direction γ.

of incidence, α, from 0 to 29.7 deg, and low Reynolds numbers Re from 1.5×10^6 to 8.5×10^6, and in the Centre d'Etudes et de Recherches de Toulouse (CERT)/ONERA F1 Wind Tunnel Le Fauga-Mauzac Center Toulouse39[50] at α from 10 to 30 deg and high Reynolds numbers Re from 6.5×10^6 to 43.5×10^6. The model was equipped with one array of pressure taps and one array of hot films, which provided skin-friction measurements in magnitude and direction. Both arrays were aligned in the streamwise direction. When rotated, the prolate spheroid around the major axis measurements in different ϕ positions were produced.

Figures 2 and 3 show a comparison of the computed pressure distribution with measurements for an angle of attack $\alpha = 10$ and 29.7 deg (Ref. 49). In Figs. 2 and 3, the C_p curve for the X station $X/a = -0.9988$ represents the correct numerical values, the remaining curves are displaced by a factor $\Delta C_p = 0.14$. The dashed line indicates the position of the computed open laminar free vortex separation line. As can be seen, the measured pressure distribution compares sufficiently well with the potential theory, except for larger values of X/a on the leeward side of the free vortex separation line. Hence, the inviscid flowfield is well represented by the potential theory in regions of attached laminar flows.

The measured[49] resultant skin friction in magnitude and direction is compared with computations for $\alpha = 10$ and 29.7 deg in Figs. 4 and 5, respectively. The Reynolds number $Re = 1.5 \times 10^6$ is the lowest Reynolds number measured, which produces the largest amount of laminar flow. In Figs. 4 and 5, C_{ft} and γ curves represent the correct numerical values for the X station $X/a = -0.894$. The remaining curves are displaced by $\Delta C_{ft} = -1.5$ and $\Delta\gamma = -15$ deg in Fig. 4 and by $\Delta C_{ft} = -3.0$ and $\Delta\gamma = -20$ deg in Fig. 5. The

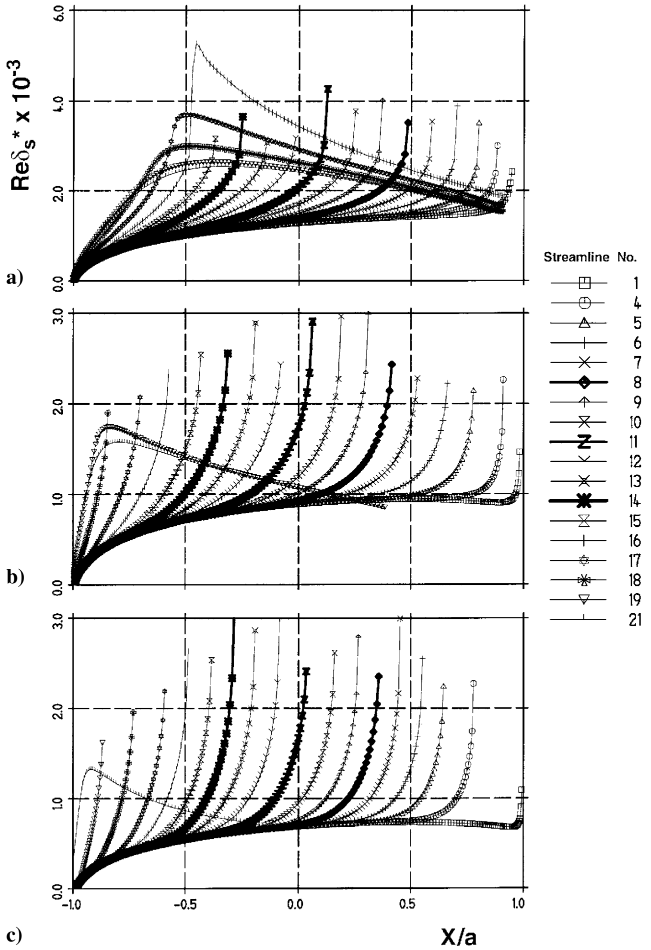

Fig. 6 Reynolds number based on displacement thickness of streamwise velocity profile along different streamlines for a) $Re = 6.56 \times 10^6$ and $\alpha = 10$ deg, b) $Re = 6.53 \times 10^6$ and $\alpha = 20$ deg, and c) $Re = 6.54 \times 10^6$ and $\alpha = 29.7$ deg.

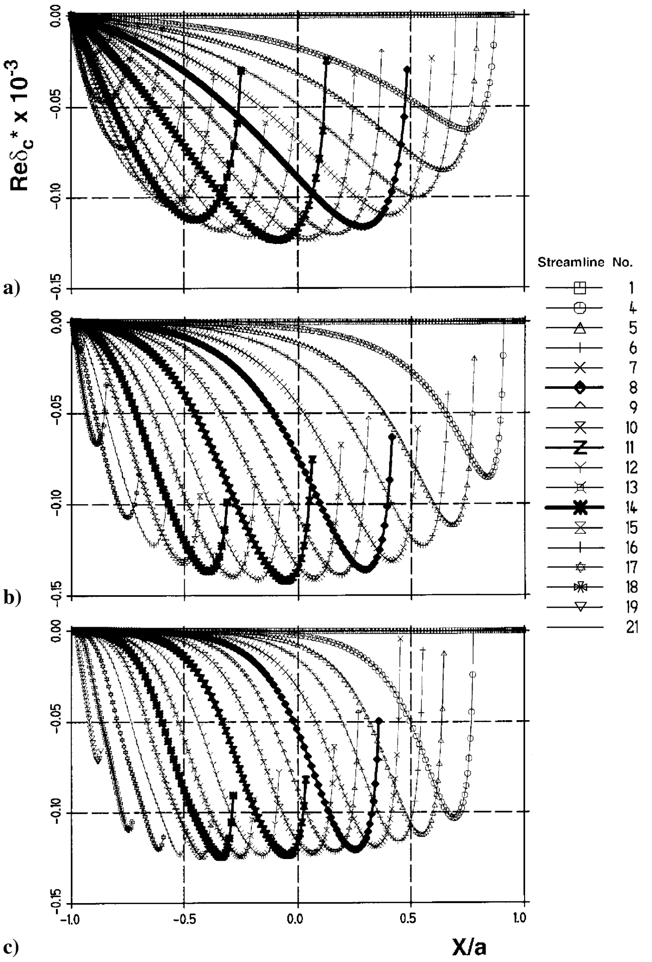

Fig. 7 Reynolds number based on displacement thickness of crossflow velocity profile along different streamlines for a) $Re = 6.56 \times 10^6$ and $\alpha = 10$ deg, b) $Re = 6.53 \times 10^6$ and $\alpha = 20$ deg, and c) $Re = 6.54 \times 10^6$ and $\alpha = 29.7$ deg.

computation produces attached laminar flow in the complete circumferential direction for the first two X stations, $X/a = -0.894$ and $X/a = -0.722$ (Fig. 4). Farther downstream, the free vortex separation is indicated on the leeward side. For the $\alpha = 29.7$ deg case, the free vortex separation starts right at the first measuring station, $X/a = -0.894$ (Fig. 5). As can be seen, the predicted values of C_{ft} and γ agree fairly well with computations, except for large values of X/a. Furthermore, the measured transition locations, which are also indicated in Figs. 4a and 5a, and the predicted separation locations are relatively close. Indeed, as documented in Sec. III.C, the boundary-layer flow is predicted to remain laminar up to the free vortex separation line for the low Reynolds numbers $Re = 1.52 \times 10^6$ in Fig. 4 and 1.53×10^6 in Fig. 5, respectively.

To conclude, the quality of the pressure and skin-friction predictions documents that the inviscid and viscous flow is described sufficiently well by potential theory and boundary-layer computations in regions of attached laminar boundary layers.

B. Boundary-Layer and Stability Results

Figures 6 and 7 show the Reynolds numbers based on the displacement thickness of the streamwise velocity profile, $Re\delta_s^*$, and based on the displacement thickness of the crossflow velocity profile, $Re\delta_c^*$, respectively. The results are shown along different streamlines up to the free vortex separation line for angles of attack $\alpha = 10$, 20, and 29.7 deg and Reynolds number $Re = 6.5 \times 10^6$. For comparison, the results for the streamline numbers 8, 11, and 14 are marked in thick lines. Streamline 1 corresponds to the windward and the streamline 21 to the leeward symmetry plane. As can be seen, the development of $Re\delta_s^*$ is very similar for all cases except close to the leeward symmetry plane. The separation moves gradually upstream from streamline 1 up to streamline 15 for $\alpha = 10$ deg, up to streamline 18 for $\alpha = 20$ deg, and up to streamline 19 for $\alpha = 29.7$ deg. Close to the leeward symmetry plane, the values of $Re\delta_s^*$ show a maximum without separating and relax in the downstream direction. The values of $Re\delta_c^*$ also appear comparable for the different angles of incidence. Detailed inspection, however, reveals that the absolute values of $Re\delta_c^*$ increase almost linearly from the start of the boundary layer for $\alpha = 10$ deg, whereas with augmenting angle of incidence, the initial increase is reduced. To the contrary, the values of $Re\delta_c^*$ grow more rapidly farther downstream for larger angles of attack.

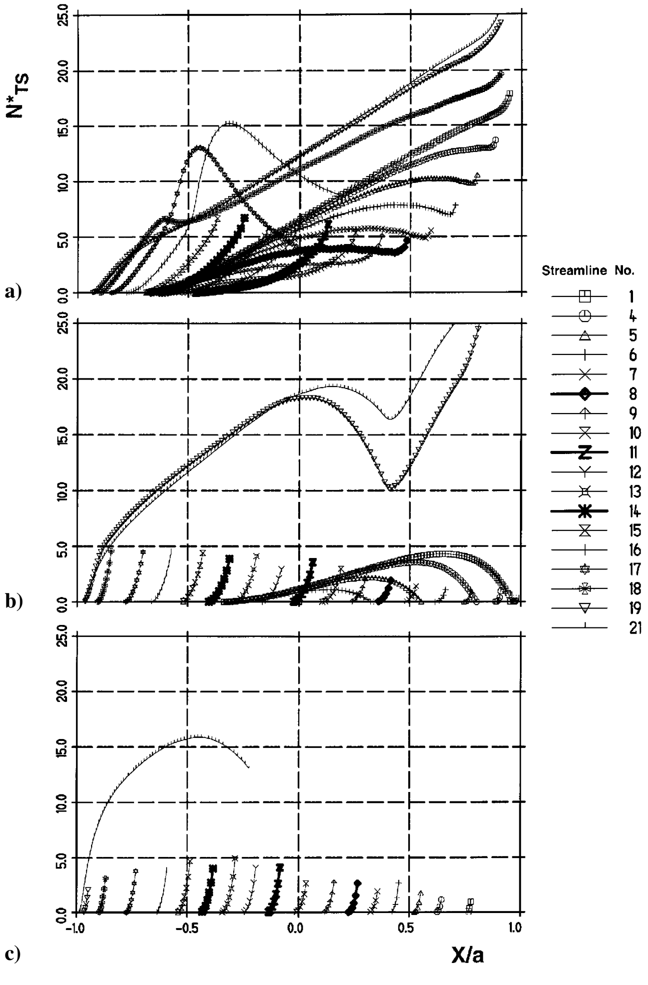

Fig. 8 Envelope N factors for TS waves along different streamlines for a) $Re = 6.56 \times 10^6$ and $\alpha = 10$ deg, b) $Re = 6.53 \times 10^6$ and $\alpha = 20$ deg, and c) $Re = 6.54 \times 10^6$ and $\alpha = 29.7$ deg.

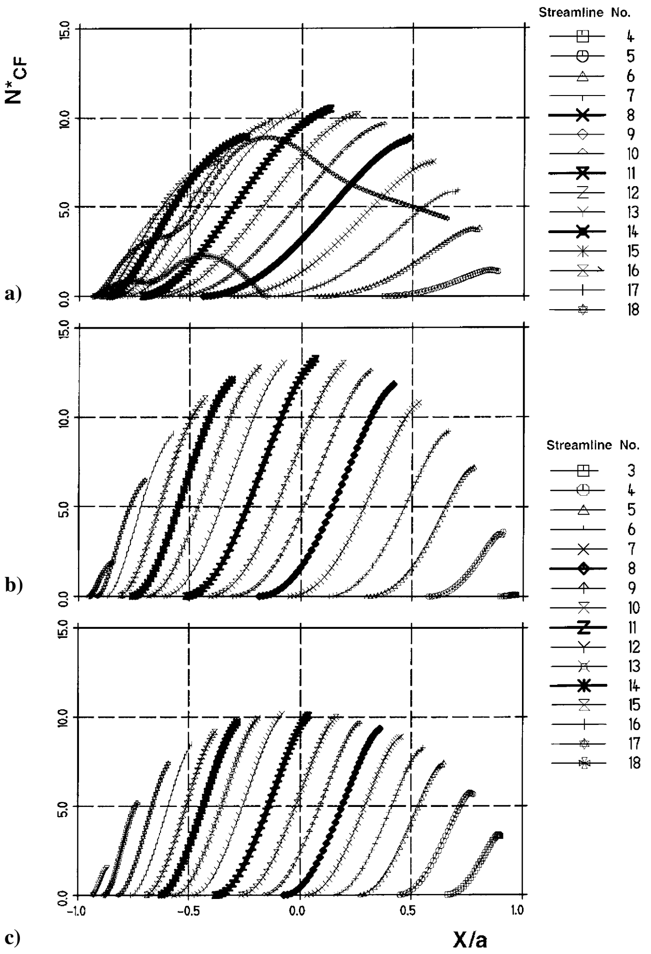

Fig. 9 Envelope N factors for crossflow waves along different streamlines for a) $Re = 6.56 \times 10^6$ and $\alpha = 10$ deg, b) $Re = 6.53 \times 10^6$ and $\alpha = 20$ deg, and c) $Re = 6.54 \times 10^6$ and $\alpha = 29.7$ deg.

The envelopes of the TS and CF waves are presented along different streamlines in Figs. 8 and 9 for the flow conditions of Figs. 6 and 7. For the $\alpha = 10$ deg case (Fig 8a), the N_{TS}^* factors achieve large values on the windward side, streamlines 1–6, and on the leeward side, streamlines 16–21. The remaining streamlines exhibit moderate N_{TS}^* factors up to separation. For the $\alpha = 20$ deg case (Fig. 8b), the streamlines on the windward side show drastically reduced N_{TS}^* factors. On the leeward side, streamlines 19–21 still produce large N_{TS}^* factor values. This tendency is even more pronounced for the $\alpha = 29.7$ deg case (Fig. 8c). The N_{TS}^* factor only shows remarkable values along the leeward symmetry plane. The N_{CF}^* factors presented in Fig. 9 appear fairly similar for all angles of attack, except on the leeward side for $\alpha = 10$ deg. Only the maximum values of N_{CF}^* initially grow slightly when α is increased from $\alpha = 10$ to 20 deg and decay slightly for $\alpha = 29.7$ deg. The crossflow wave excitation starts (neutral point) farther downstream for increased angles of attack, but the growth rate of the N_{CF}^* factors is increased, at separation achieving comparable values of N_{CF}^*. The influence

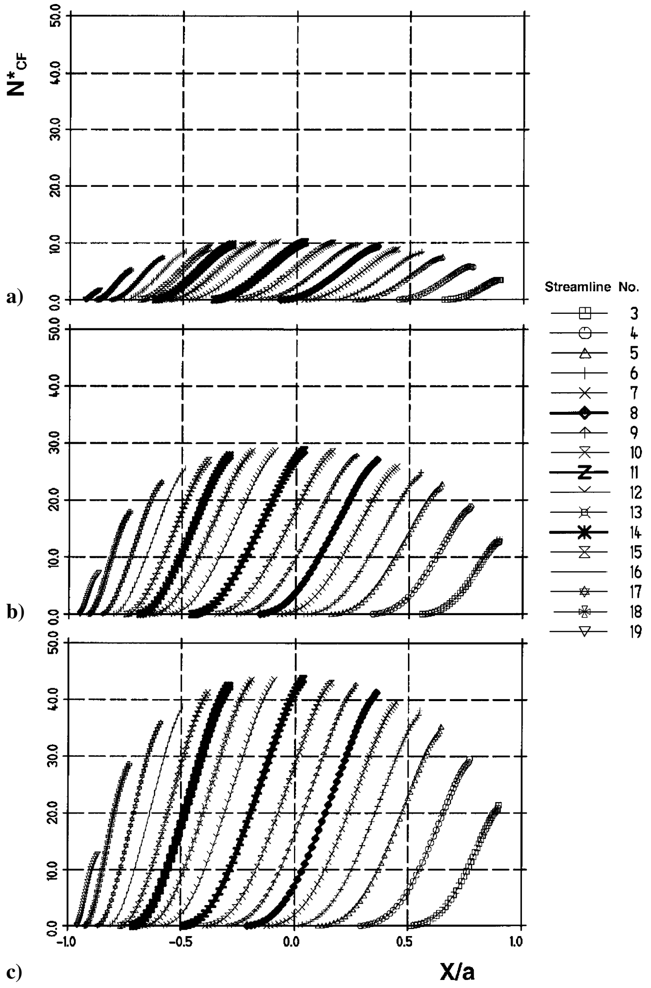

Fig. 10 Envelope N factors for crossflow waves along different streamlines for angle of attack $\alpha = 30$ deg and a) $Re = 6.65 \times 10^6$, b) $Re = 23.96 \times 10^6$, and c) $Re = 43.54 \times 10^6$.

of the Reynolds number on the N^*_{CF} factor is shown in Fig. 10 for angle of attack $\alpha = 30$ deg and Reynolds numbers $Re = 6.65 \times 10^6$, 23.96×10^6, and 43.54×10^6. As can be seen, the maximum values of N^*_{CF} increase drastically from 10 to 45 from the lowest to the highest Reynolds number, respectively. Furthermore, the location where the instablities start is moving upstream for increasing Reynolds numbers.

The N^*_{TS} and N^*_{CF} factor values at measured transition, N_{TS} and N_{CF}, respectively, are presented for the tests in the DFVLR 3 × 3 Meter Low Speed Wind Tunnel Göttingen[49] in Fig. 11. The results in Figs. 11a and 11b are given for pure TS and pure CF wave excitation, respectively. The number of data points, where both waves are amplified, is fairly small (Fig. 11c). The small scatter of data in Figs. 11a and 11b clearly permits the determination of the limiting N factors, $N_{TS} = 8.0$ and $N_{CF} = 5.5$. To the contrary, the scatter is fairly large for simultaneously excited TS and CF waves (Fig. 11c). Because the computational results so far presented are evaluated without curvature effects, the scatter for simultaneously excited TS and CF waves now may be reduced by taking curvature effects into account. The result for CF waves is presented in Fig. 12; TS waves are not affected by curvature. As can seen, the values of N_{CF} vary randomly between 0 and 4.0, such that a correlation for the limiting N factor of CF waves cannot be found. For that reason, all further stability computations are executed without curvature effects. The final stability limit is shown in the N_{TS}–N_{CF} diagram (Fig. 11c). For N_{CF} values < 1.0, the limiting N factor for TS waves remains $N_{TS} = 8.0$, and similarly for N_{TS} values < 1.0, the limiting N factor for crossflow waves remains $N_{CF} = 5.5$. In between, N_{TS} is assumed to decay linearly with increasing values of N_{CF}, which reduces the stable region for simultaneously excited TS and CF waves. This reduction tries to model the interaction of TS and CF waves, which cannot be evaluated by the local, linear stability theory. The actual reduction for prolate spheroids is by far larger when compared to the reduction for infinite swept wing configurations.[43] Apparently, the interaction of TS and CF waves is more intensified in fully three-dimensional boundary layers. The corresponding results for the measurements in the CERT/ONERA F1 Wind Tunnel Le Fauga-Mauzac Center

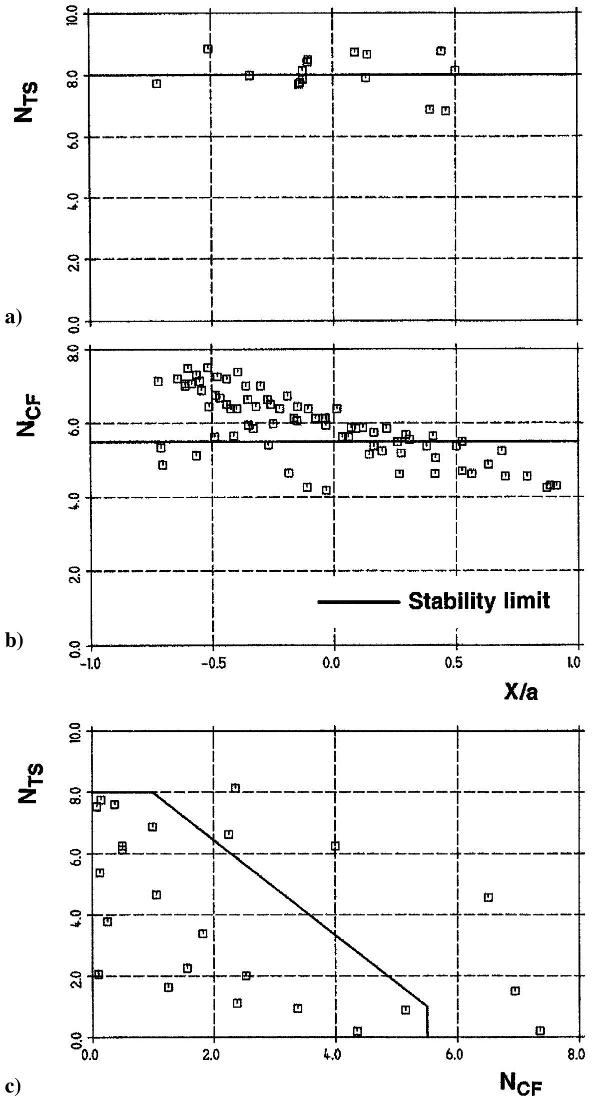

Fig. 11 N_{TS} and N_{CF} values at measured transition locations[49]: a) N_{TS} vs X/a, b) N_{CF} vs X/a, and c) stability diagram N_{TS} vs N_{CF}.

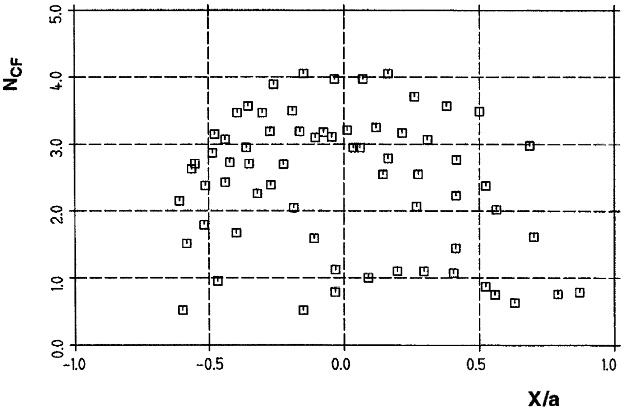

Fig. 12 N_{CF} values at measured transition locations[49] with curvature included in stability computations.

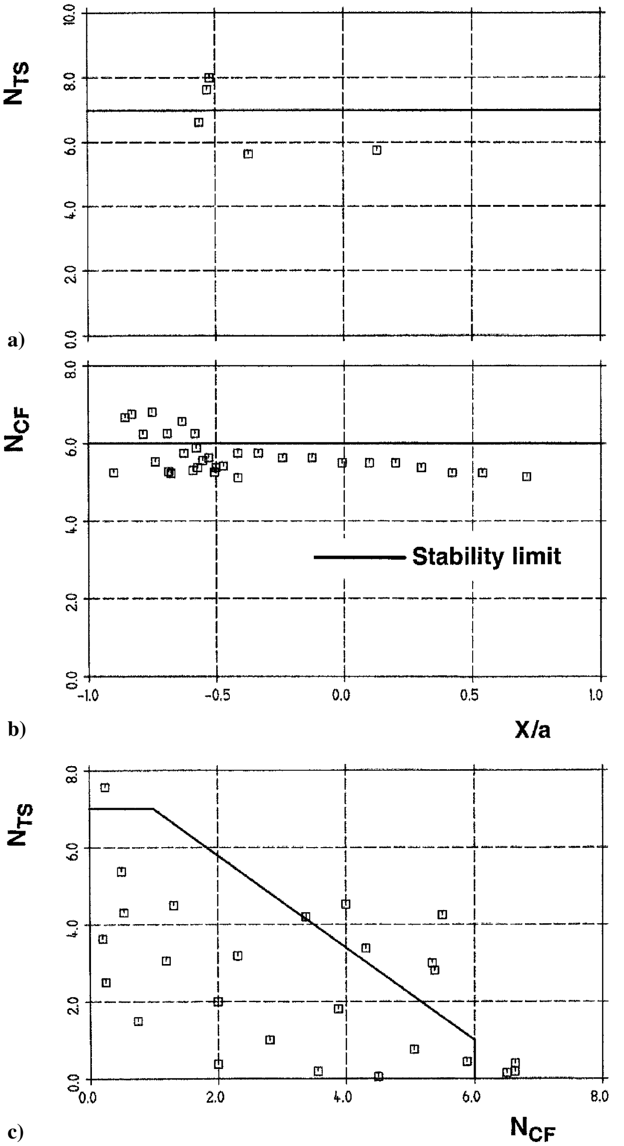

Fig. 13 N_{TS} **and** N_{CF} **values at measured transition locations**[50]**: a)** N_{TS} **vs** X/a**, b)** N_{CF} **vs** X/a**, and c) stability diagram** N_{TS} **vs** N_{CF}**.**

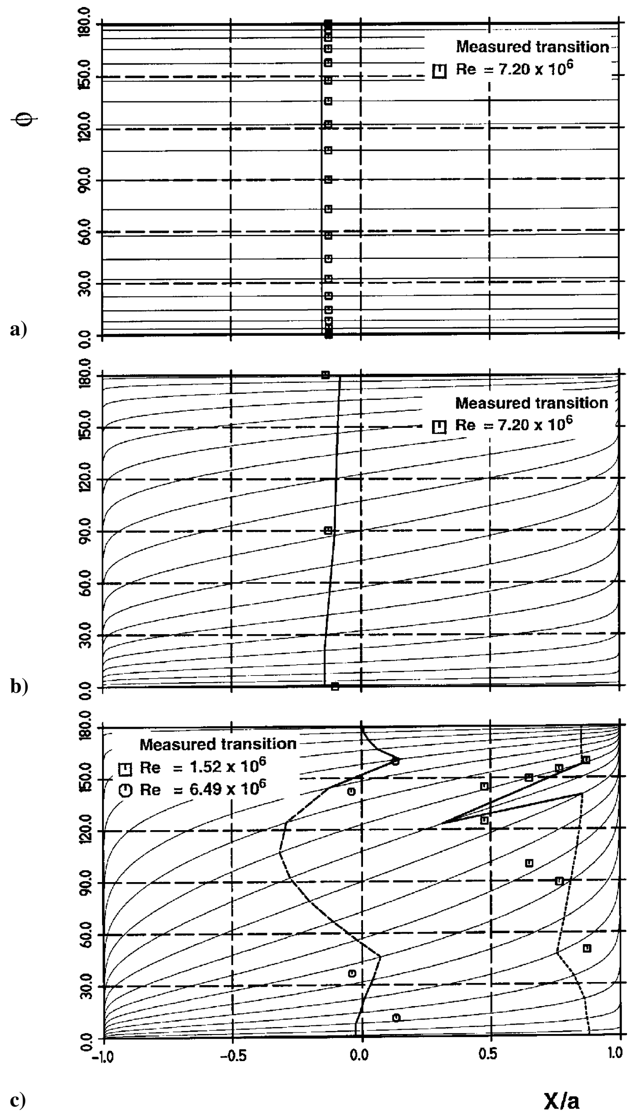

Fig. 14 Comparison of measured[49] **and computed transition locations for angle of attack: a)** $\alpha = 0$ **deg, b)** $\alpha = 2.5$ **deg, and c)** $\alpha = 5$ **deg: ——, streamlines; - - - -, free vortex-layer separation; ▬▬, TS waves; and – – –, TS and CF waves.**

Toulouse[50] are presented in Fig. 13. The overall behavior is fairly similar to that of the preceding wind-tunnel studies, although the investigated Reynolds numbers are considerably higher. The limiting N factors are slightly different, $N_{TS} = 7.0$ and $N_{CF} = 6.0$, respectively.

The infinite swept wing equipped with the ONERA D profile and cambered leading edge, tested in the CERT/ONERA F1 Wind Tunnel, was investigated in Ref. 43. The limiting N factors for that wing configuration were shown to be identical, $N_{TS} = 7.0$ and $N_{CF} = 6.0$, respectively. Hence, this outcome gives further support to the applicabilty of the e^N method because the tested models were completely different.

C. Predicted Transition

The transition prediction process differentiates in Figs. 14–17 between pure TS waves produced transition (continuous line), pure CF waves triggered transition (long dashed lines), transition provoked by both types of waves (midsized dashed lines), and separation (short dashed lines). The measured transition locations are now compared with transition predictions in Figs. 14–16 for the wind-tunnel tests of Ref. 49 and in Fig. 17 for the tests of Ref. 50. Figure 14 gives the results for angles of incidence, $\alpha = 0$, 2.5, and 5 deg. Transition is provoked solely by TS waves for $\alpha = 0$ and 2.5 deg and a Reynolds number $Re = 7.2 \times 10^6$ (Figs. 14a and 14b). The results for $\alpha = 5.0$ deg and Reynolds numbers $Re = 1.52 \times 10^6$ and 6.49×10^6 is shown in Fig. 14c. The flow is predicted to remain laminar up to separation for the small-Reynolds-number case, except for streamline 12, where transition is provoked by TS waves. In the actual case, the boundary layer is drastically thickened in the neighborhood of streamline 12 by the action of the circumferential pressure gradient, as already mentioned in Sec. II.B. The measured transition line shows a fairly similar behavior. For the higher-Reynolds-number case, transition is triggered by TS waves near the windward and leeward symmetry planes and for the remaining part of the body surface simultaneously by TS and CF waves. Figure 15 shows the results for $\alpha = 10$, 15, and 20 deg. The boundary-layer flow is predicted to stay laminar up to separation for $\alpha = 10$ deg and a Reynolds number $Re = 1.52 \times 10^6$ (Fig. 15a). Indeed, the measured transition locations show the same tendency. The transition locations are fairly well predicted for the higher Reynolds number $Re = 6.56 \times 10^6$. Close to the symmetry planes, pure TS waves dominate, followed in both directions by simultaneous TS and CF waves, which produced transition. In the middle part of the prolate spheroid, pure CF wave triggering is present. In Fig. 15b, the transition region provoked by simultaneous TS and CF waves is clearly reduced, wheras the region with pure CF wave-triggered transition is enlarged. Finally, in Fig. 15c for $\alpha = 20$ deg,

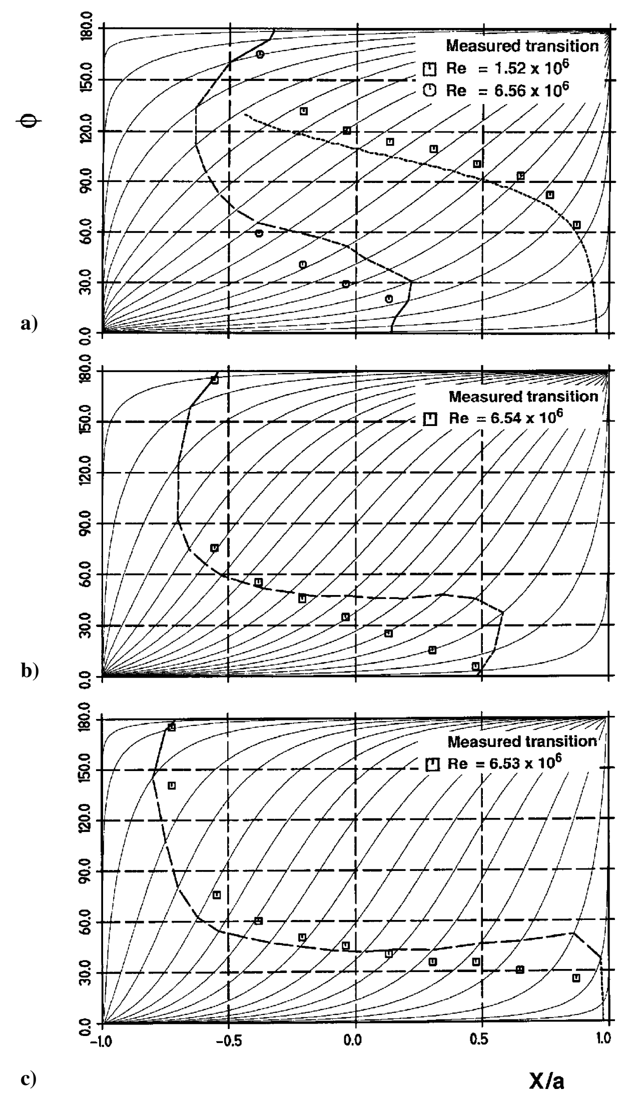

Fig. 15 Comparison of measured[49] and computed transition locations for angle of attack a) $\alpha = 10$ deg, b) $\alpha = 15$ deg, and c) $\alpha = 20$ deg: ——, streamlines; - - - -, free vortex-layer separation; ▬▬, TS waves; – – –, TS and CF waves; and — —, CF waves.

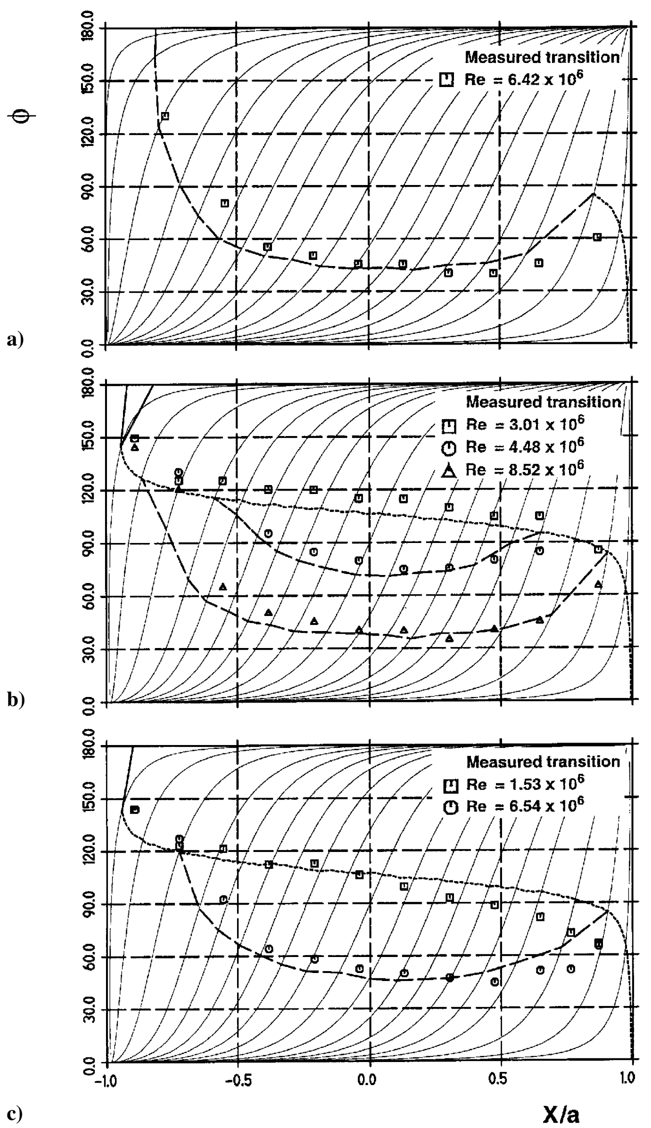

Fig. 16 Comparison of measured[49] and computed transition locations for angle of attack a) $\alpha = 24$ deg, b) $\alpha = 29.5$ deg, and c) $\alpha = 29.7$ deg: ——, streamlines; - - - -, free vortex-layer separation; ▬▬, TS waves; – – –, TS and CF waves; and — —, CF waves.

the process of TS and CF waves-produced transition is no longer existent.

Flow separation is indicated for the first time at the rear end of the prolate spheroid on the windward symmetry plane for $\alpha = 20$ deg and for $\alpha > 20$ deg shown in Figs. 14–17. In Fig. 16 the results are shown for $\alpha = 24$, 29.5, and 29.7 deg. Transition appears to be produced solely by CF waves except close to the leeward symmetry planes for $\alpha = 24$ deg (Fig. 16a). Figure 16b shows the results for $\alpha = 29.5$ deg for three different Reynolds numbers, $Re = 3.01 \times 10^6$, 4.48×10^6, and 8.52×10^6. For the smallest Reynolds number, the flow remains laminar up to separation. The prediction clearly follows the tendency of the measurements. For the remaining Reynolds numbers, transition is triggered by CF waves, except close to the symmetry planes. On the leeward symmetry plane, transition is provoked by TS waves, where transition is predicted farther upstream for the higher Reynolds number, followed by a small region of separated flow, and close to the windward symmetry plane by separation. The measured reduction of the laminar flow region by the Reynolds number increase is excellently reproduced by the computations. The transition prediction for $\alpha = 29.7$ deg and two Reynolds numbers (Fig. 16c) is of similar quality. For the small Reynolds number, transition is provoked completely by separation.

Figure 17 shows the results for the wind-tunnel tests of Ref. 50. The high Reynolds number possibilities in the pressurerized facility were the main argument for this wind-tunnel campaign aside from comparison purposes. Figure 17 comprises the results for $\alpha = 10, 15$, and 30 deg. The predicted transition locations presented in Figs. 17a and 17b, are comparable to those of Ref. 49 (Fig. 15), except for the high-Reynolds-number case in Fig. 17a. The latter is in good agreement with the actual experimental observations. In Fig. 17c, comparisons are shown for three Reynolds numbers, $Re = 6.65 \times 10^6$, 23.96×10^6, and 43.54×10^6, where the latter two Reynolds numbers are the highest measured. The experimentally observed migration of the transition line due to the Reynolds number increase is almost identically reproduced by the computations.

Finally, Fig. 18 shows the computed variation of the transition line for comparable Reynolds numbers $Re = 7.2 \times 10^6$ for $\alpha = 0$ and 2.5 deg and Reynolds numbers from 6.40×10^6 to 6.54×10^6 for α from 5 to 29.7 deg. Increasing the angle of attack moves transition continously downstream on the windward symmetry plane and continously upstream on the leeward symmetry plane for $\alpha > 5$ deg. There exists a distinct zone in the lower-half of the prolate spheroid around $\phi = 50$ deg, which separates the downstream and upstream motion of the transition line. Along this line, the transition locations are almost identical for angles of incidence α from 15 to 29.7 deg between $X/a = -0.5$ and $X/a = 0.5$.

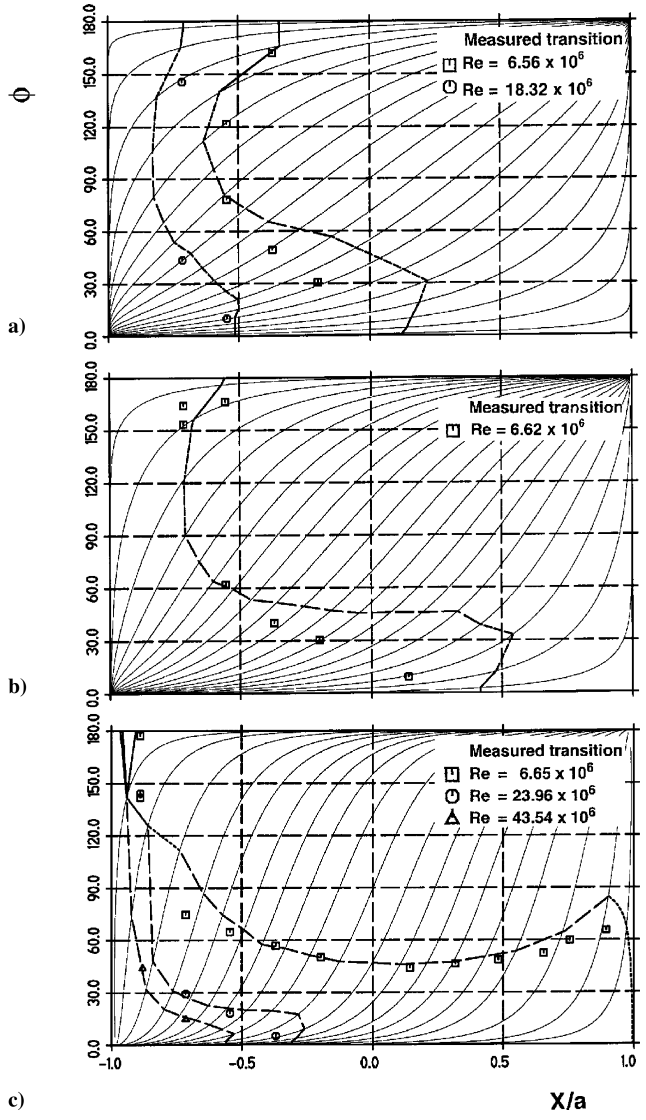

Fig. 17 Comparison of measured[50] and computed transition locations for an angle of attack a) $\alpha = 10$ deg, b) $\alpha = 15$ deg, and c) $\alpha = 30$ deg: ——, streamlines; - - - -, free vortex-layer separation; ▬▬, TS waves; – – –, TS and CF waves; and ——–, CF waves.

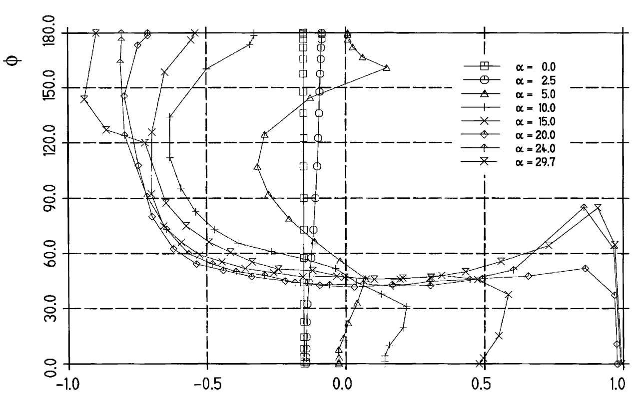

Fig. 18 Computed transition location for different angles of attack and comparable Reynolds numbers: for $\alpha = 0$ and 2.5 deg, $Re = 7.2 \times 10^6$ and for $\alpha = 5$–29.7 deg, $Re = 6.40 \times 10^6$–6.54×10^6.

IV. Conclusions

The main emphasis of the present study is to prove the applicability of the e^N method in complex three-dimensional boudary-layer flows. The flow around inclined prolate spheroids is investigated, which produces highly divergent and convergent boundary layers on curved surfaces. The inviscid flowfield is calculated by the potential theory and the viscous flows by a finite difference method for three-dimensional, laminar boundary layers. This approach is shown to compare well with measured wall pressures and skin friction in magnitude and direction, when restricted to attached laminar flow. The laminar boundary layer is analyzed by the local, linear stability method, applying the two N factor e^N method. The N factor integration of both TS and CF waves is executed along 21 inviscid streamlines, which regularly cover the surface of the prolate spheroid. The N factor computations are executed with and without body curvature effects. It is clearly shown that the computation with curvature effects included produces results for which a comprehensive stability limit cannot be found. To the contrary, the values of the N factors without curvature effects exhibit, at the measured transition locations for all investigated angles of incidence and Reynolds numbers, such a small scatter that the limiting N factors for both types of waves can be determined with confidence. The limiting N factors, which represent the stability limit of the prolate spheroid in the considered wind tunnel, are finally introduced to predict the transition location. The important outcome for two wind-tunnel campaigns is the satisfactory agreement between measured and predicted transition locations, particularly, when considering the large range of angles of incidence, α from 0 to 30 deg, and of Reynolds number, from 1.5×10^6 to 43.5×10^6. Hence, it is clearly documented that the e^N method is very applicable for transition prediction in complex, three-dimensional, laminar boundary layers.

Acknowledgments

The author thanks Jean Cousteix and Daniel Arnal from Centre d'Etudes et de Recherches de Toulouse (CERT)/ONERA in Toulouse, France, for the delivery of their three-dimensional boundary-layer code and Robert Houdeville from CERT/ONERA for his valuable advice on the application of the boundary-layer code. Furthermore, the author is very grateful to Hans Peter Kreplin from the DLR, German Aerospace Center, Göttingen, Germany, for reports of the prolate spheroid measurements in the 3 × 3 Meter Low Speed Wind Tunnel at the DLR Göttingen and in the CERT/ONERA F1 Wind Tunnel Le Fauga-Mauzac Center, Toulouse.

References

[1] Morkovin, M. V., "On the Many Faces of Transition," *Viscous Drag Reduction*, edited by C. S. Wells, Plenum, New York, 1969, pp. 1–31.

[2] Mayle, R. E., and Schulz, A., "The Role of Laminar–Turbulent Transition in Gas Turbine Engines," *Journal of Turbomachinery*, Vol. 113, March 1991, pp. 509–537.

[3] Reed, H. L., Haynes, T. S., and Saric, W. S., "Computational Fluid Dynamics Validation Issues in Transition Modeling," *AIAA Journal*, Vol. 36, No. 5, 1998, pp. 742–751.

[4] Durbin, P. A., Jacobs, R. G., and Wu, X., "DNS of Bypass Transition," *Closure Strategies for Turbulent and Transitional Flows*, edited by B. E. Launder and N. B. Sandsam, Cambridge Univ. Press, London, 2002, pp. 449–463.

[5] Menter, F. R., Langtry, R., Völker, S., and Huang, P. G., "Transition Modelling for General Purpose CFD Codes," *Engineering Turbulence Modelling and Experiments 6*, edited by W. Rodi and M. Mulas, Elsevier Sciences, Oxford, 2005, pp. 31–46.

[6] Wilcox, D. C. W., "Simulation of Transition with a Two-Equation Turbulence Model," *AIAA Journal*, Vol. 32, No. 2, 1994, pp. 247–255.

[7] Warren, E. S., and Hassan, H. A., "Transition Closure Model for Predicting Transition Onset," *Journal of Aircraft*, Vol. 35, No. 5, 1994, pp. 769–775.

[8] Edwards, J. R., Roy, C. J., Blottner, F. G., and Hassan, H. A., "Development of a One-Equation Transition/Turbulence Model," *AIAA Journal*, Vol. 39, No. 9, 2001, pp. 1691–1698.

[9] Steelant, J., and Dick, E., "Modelling of Laminar–Turbulent Transition for High Freestream Turbulence," *Journal of Fluids Engineering* , Vol. 123, No. 1, 2001, pp. 22–30.

[10] Langtry, R. B., and Menter, F. R., "Transition Modeling for General CFD Applications in Aeronautics," AIAA Paper 2005-522, Jan. 2005.

[11] Smith, A. M. O., and Gamberoni, N., "Transition, Pressure Gradient and Stability Theory," Douglas Aircraft Co., Rept. ES 26388, Long Beach, CA, Sept. 1956.

[12] van Ingen, J. L., "A Suggested Semi-Empirical Method for the Calculation of the Boundary Layer Transition Region," Dept. of Aerospace Engineering, Rept. VTH-74, Univ. of Delft, Delft, The Netherlands, Nov. 1956.

[13] Arnal, D., and Casalis, G., "Laminar–Turbulent Transition Prediction in Three-Dimensional Flows," *Progress in Aerospace Sciences*, Vol. 36, March 2000, pp. 173–191.

[14] Crouch, J. D., Crouch, I. W. M., and Ng, L. L., "Transition Prediction for Three-Dimensional Boundary Layers in Computational Fluid Dynamics Application," *AIAA Journal*, Vol. 40, No. 8, 2002, pp. 1536–1541.

[15] Horstmann, K. H., Quast, A., and Redeker, G., "Flight and Wind-Tunnel Investigations on Boundary-Layer Transition," *Journal of Aircaft*, Vol. 27, No. 2, 1990, pp. 146–150.

[16] Horstmann, K. H., and Körner, H., "Natural Laminar Flight Test Investigation for Commuter Aircraft Application," Association Aeronautique et Astronautique de France, 2nd European Forum on Laminar Flow Technology, Paper 2.3, June 1996.

[17] Horstmann, K. H., Müller, R., Dick, P., and Wohlrath, W., "Flugversuche am Laminarhandschuh der Do228," Deutsche Gesellschaft für Luft- und Raumfahrt, Rept. DGLR-Bericht 92-07, Braunschweig, Germany, Nov. 1992.

[18] Wohlrath, W., Echtle, H., Dick, P., Welte, D., Stock, H. W., Moeken, B., Horstmann, K. H., Müller, R., Rohardt, C. H., and Quast, A., "Design and Flight Test Evaluation of a Laminar Wing Glove on a Commuter Aircraft," International Council of the Aeronautical Sciences, Paper 94-5.4.1, June 1994.

[19] Schrauf, G., "Transition Prediction Using Different Linear Stability Analysis Strategies," AIAA Paper 94-1848, June 1994.

[20] Henke, R., Münch, F. X., and Quast, A., "Natural Laminar Flow: A Wind Tunnel Test Campaign and Comparison with Free Flight Test Data," AIAA Paper 90-3045, Aug. 1990.

[21] Horstmann, K. H., Redeker, G., Quast, A., Dressler, U., and Bieler, H., "Flight Tests with a Natural Laminar Flow Glove on a Transport Aircraft," AIAA Paper 90-3044, Aug. 1990.

[22] Schrauf, G., Perraud, J., and Lam, F., "Comparison of Boundary-Layer Transition Predictions Using Free Flight Test Data," *Journal of Aircraft*, Vol. 35, No. 6, 1998, pp. 891–897.

[23] Schrauf, G., "Linear Stability Theory Applied to Wind Tunnel and Flight Experiments," *Proceedings of the 4th European Computational Conference, ECCOMAS 98*, Vol. 2, Wiley, Chichester, England, U.K., 1998, pp. 126–131.

[24] Schrauf, G., Perraud, J., Lam, F., Stock, H. W., Vitiello, D., and Abbas, A., "Transition Prediction with Linear Stability Theory—Lessons Learned from the ELFIN F100 Flight Demonstrator," Association Aeronautique et Astronautique de France, 2nd European Forum on Laminar Flow Technology, Paper 8.5, June 1996.

[25] Arnal, D., and Bulgubure, C., "Drag Reduction by Boundary-Layer Laminarisation," *La Recherche Aerospatiale*, Vol. 23, No. 3, 1996, pp. 157–165.

[26] Mullender, A. J., and Riedel, H., "A Laminar Flow Nacelle Flight Test Programme," Association Aeronautique et Astronautique de France, 2nd European Forum on Laminar Flow Technology, Paper 2.4, June 1996.

[27] Riedel, H., Horstmann, K. H., Ronzheimer, A., and Sitzmann, M., "Aerodynamic Design of a Natural Laminar Flow Nacelle and the Design Validation by Flight Testing," *Aerospace Science and Technology*, Vol. 1, No. 1, 1998, pp. 1–12.

[28] Redeker, G., Horstmann, K. H., Köster, H., Thiede, P., and Szodruch, J., "Design of a Natural Laminar Flow Glove for a Transport Aircraft," AIAA Paper 90-3043, Aug. 1990.

[29] Dressler, U., Hansen, H., Rill, S., Horstmann, K. H., Rohardt, C. H., and Wichmann, G., "Design of the Fokker F100 Natural Laminar Flow Glove," Deutsche Gesellschaft für Luft- und Raumfahrt, Rept. DGLR-Bericht 92-06, Braunschweig, Germany, Nov. 1992, pp. 152–163.

[30] Stuke, H., Preist, J., and Capbern, P., "Principles of Aerodynamic Layout and Design of a Demonstrator Suction System," Association Aeronautique et Astronautique de France, 2nd European Forum on Laminar Flow Technology, Paper 6.4, June 1996.

[31] Mullender, A. J., Lecordix, J. L., Lecossais, E., Godard, J. L., and Hepperle, M., "The ELFIN II and LARA HLF Nacelles: Design, Manufacture and Test," Association Aeronautique et Astronautique de France, 2nd European Forum on Laminar Flow Technology, Paper 5.3, June 1996.

[32] Radespiel, R., Horstmann, K. H., and Redeker, G., "Feasibility Study on the Design of a Laminar Flow Nacelle," *Journal of Aircraft*, Vol. 27, No. 11, 1990, pp. 959–965.

[33] Köster, H., and Müller, R., "Bestimmung des N-Faktors im Transsonischen Wind-kanal Braunschweig (TWB) anhand von Druckverteilungs- und Umschlagspunktmessungen und dem Sally-Verfahren," Deutsche Gesellschaft für Luft- und Raumfahrt, Rept. DGLR-Bericht 88-05, Braunschweig, Germany, Nov. 1988, pp. 66–77.

[34] Gaudet, L., Betts, C. J., and Ashill, P. R., "Experimental Investigation of Boundary Layer Transition on a Natural Laminar Flow Airfoil," Deutsche Gesellschaft für Luft- und Raumfaht, Rept. DGLR-Bericht 92-06, Braunschweig, Germany, Nov. 1992, pp. 132–140.

[35] Dagenhart, J. R., "Cross-Flow Stability and Transition Experiments in a Swept Wing Flow," NASA TM 108650, Feb. 1992.

[36] Stock, H. W., and Haase, W., "Feasibilty Study of e^N Transition Prediction in Navier–Stokes Methods for Airfoils," *AIAA Journal*, Vol. 37, No. 10, 1999, pp. 1187–1196.

[37] Stock, H. W., and Haase, W., "Navier–Stokes Airfoil Computations with e^N Transition Prediction Including Transitional Flow Regions," *AIAA Journal*, Vol. 38, No. 11, 2000, pp. 2059–2066.

[38] Stock, H. W., "Airfoil Validation Using Coupled Navier–Stokes and e^N Transition Prediction Methods," *Journal of Aircraft*, Vol. 39, No. 1, 2002, pp. 51–58.

[39] Stock, H. W., "Wind-Tunnel-Flight Correlation for Laminar Wings in Adiabatic and Heating Flow Conditions," *Aerospace Science and Technology*, Vol. 6, June 2002, pp. 245–257.

[40] Rozendaal, R. A., "Natural Laminar Flow Flight Experiments on a Swept Wing Business Jet—Boundary-Layer Stability Analysis," NASA CP-3975, March 1986.

[41] Rozendaal, R. A., "Variable-Sweep Transition Flight Experiment (VSTFE)—Parametric Pressure Distribution Boundary-Layer Stability Study and Wing Glove Design Task," NASA CR 3992, Dec. 1986.

[42] Rozendaal, R. A., "Variable-Sweep Transition Flight Experiment (VSTFE)—Stability Code Development and Clean-Up Glove Analysis," NASA CP-2847, April 1987.

[43] Stock, H. W., "Infinite Swept Wing Navier–Stokes Computations with e^N Transition Prediction," *AIAA Journal*, Vol. 43, No. 6, 2005, pp. 1221–1229.

[44] Stock, H. W., and Seitz, A., "Crossflow Induced Transition Prediction Using Coupled Navier–Stokes and e^N Method Computations," *AIAA Journal*, Vol. 42, No. 9, 2004, pp. 1746–1754.

[45] Lamb, H., *Hydrodynamics*, Cambridge Univ. Press, London, 1932, pp. 123–126.

[46] Houdeville, R., and Malecki, P., "Calculs de Couches Limites Tridimensionelles-Description et Mode d'Emploi du Code 3C3D," Ver. 5.3, Departement d'Etudes et de Recherche en Aerothermodynamique, Rapport Technique, DERAT No. 65/5625.60, Centre d' Etudes et de Recherches de Toulouse/ONERA, Toulouse, France, Jan. 1996.

[47] Schrauf, G., "An Efficient Solver of the Eigenvalue Problem of the Linear Stability Equations for Three-Dimensional, Compressible Boundary Layer Flows," *6th DGLR–Fach–Symposium (Strömungen mit Ablösung)*, DLR, German Aerospace Center, Göttingen, Germany, 1988, pp. 18–27.

[48] Stock, H. W., "Infinite Swept Wing RANS Computations with e^N Transition Prediction-Feasibilty Study," DLR, German Aerospace Center, DLR-Interner Bericht 124-2003/12, Braunschweig, Germany, Aug. 2002.

[49] Kreplin, H. P., Vollmers, H., and Meier, H. U., "Wall Shear Stress Measurements on an Inclined Prolate Spheroid in the DFVLR 3M × 3M Low Speed Wind Tunnel, Göttingen," DFVLR-AVA, Rept. IB 222-84 A 33, Göttingen, Germany, Jan. 1985.

[50] Kreplin, H. P., Vollmers, H., and Meier, H. U., "Wall Shear Stress Measurements on an Inclined Prolate Spheroid in the ONERA F1 Wind Tunnel," DFVLR-AVA, Rept. IB 222-84 A 34, Göttingen, Germany, June 1985.

R. So
Associate Editor